SIGNATURES OF MOVING TARGET IN POLAR FORMAT SPOTLIGHT SAR IMAGE

X. H. Mao, D. Y. Zhu, and Z. D. Zhu

Department of Electronic Engineering
Nanjing University of Aeronautics and Astronautics
Nanjing, China

Abstract—The synthetic aperture radar (SAR) signatures of moving target are the basis of ground moving target detection and imaging (GMTI&Im). However, previous studies are mainly based on the 2-D separable SAR processing, and little work has been done to investigate the signatures of moving target after the application of a particular fine resolution SAR image formation algorithm. In this paper, the spectrum of moving target after polar format algorithm (PFA) processing is derived. Based on this spectrum, detailed analysis on the SAR signatures of moving target, including the geometric displacement, residual range migration, and the defocusing effect in both range and azimuth dimensions are performed. Simulation results validate the theoretical analysis.

1. INTRODUCTION

Synthetic aperture radar (SAR) is a coherent imaging technique capable of generating fine resolution images of stationary target on the ground, and it becomes an important tool in military intelligence, surveillance, and reconnaissance [1–7]. With the advancement of sophisticated SAR signal processing and imaging methods, more specialized radar problems are being studied in the framework of SAR systems. A prominent example is ground moving target detection and imaging (GMTI&Im) in a SAR scene. As is well known when a conventional SAR processing algorithm is applied to a scene containing moving targets, the images of moving targets are typically mislocated and smeared out due to the additional phase error and range migration induced by the target's motion. Therefore a prediction of the

---

Corresponding author: X. H. Mao (xinhua@nuaa.edu.cn).

response of the SAR processing algorithm employed to the SAR echo, including the geometric displacement, residual range migration and the defocusing effect in both the range and azimuth dimensions, might be helpful to improve the performance of a SAR/GMTI&Im system. For example, the geometric displacement is the basis of the moving target relocation in SAR image, and the elimination of the moving target's additional range migration is vital to improve the SCR (signal to clutter ratio) in target detection and refocus.

However, previous studies are mainly discussed in 2-D separable SAR processing framework [8–10]. In 2-D separable SAR processing, the additional range migration and high order phase error caused by target's motion are not treated at all. However, due to the similarity on echo phase between the moving target and stationary one [11], after high resolution SAR processing, the additional range migration and phase error can be partly corrected. In the past years, the image spectrum of moving target after some specific high resolution SAR image formation algorithms (RMA and BP [12, 13]) is derived, in these references, the SAR signatures are also briefly presented. However, to the author's knowledge, until recently, little work is available in the literature on the complete signatures of moving target after high resolution SAR processing. The purpose of this paper is to develop the SAR image spectrum of moving target after polar format algorithm (PFA) processing, and give a detail description of its signatures.

2. THE IMAGE-ERROR-SPECTRUM MODEL OF MOVING TARGET

Consider a spotlight SAR operating in the geometry of Fig. 1, for simplicity, we only examine the case in which the sensor travels along a straight line at constant forward velocity V_0 and radar operates in broadside mode. The central point of the scene is defined as the origin of the coordinate system, and radar antenna phase center (APC) is identified by vector $\vec{R}_a\,(u, Y_0, Z_0)$, where Y_0 and Z_0 keep constant in this geometry. Let t represent the slow time, then $u = V_0 t$ is the along track position in the X axis. The variables θ and φ are the APC's instantaneous squint angle and grazing angle, respectively, and they equal θ_0 and φ_0 at the center of the aperture.

For a point scatter target, after matched filtering, the 2-D echo signal is expressed as

$$S\,(u, f_\tau) = C \cdot \exp\left\{-j\frac{4\pi\,(f_c + f_\tau)}{c}R_t\,(u)\right\}. \qquad (1)$$

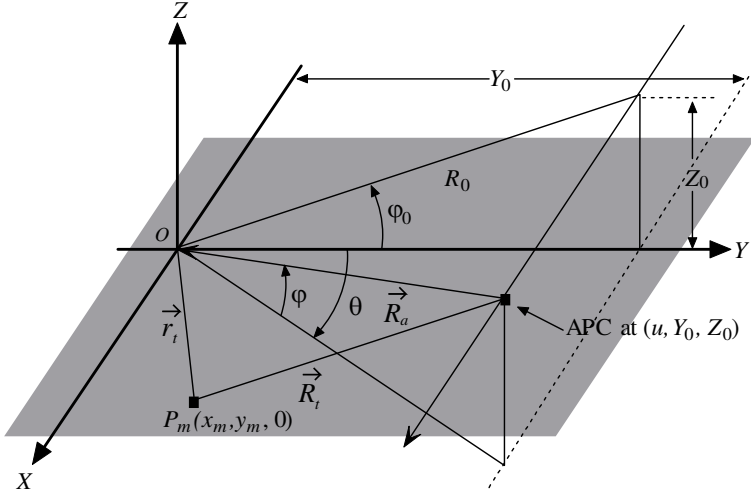where c is the velocity of propagation, f_c is the radar carrier frequency,

Figure 1. Spotlight SAR data collection geometry.

f_τ is the range frequency, C includes the nonessential factors of transmitted pulse envelop and azimuth antenna pattern, $R_t(u)$ is the instantaneous distance of target from the radar.

Furthermore, after motion compensation to the scene center, the echo signal becomes

$$S(u, f_\tau) = C \cdot \exp\left\{ j\frac{4\pi(f_c + f_\tau)}{c} R_\Delta \right\} \tag{2}$$

where $R_\Delta = R_a(u) - R_t(u)$ is the differential range.

2.1. Moving Target Model

Consider a point scatter target p_m moving at constant velocity (V_x, V_y) in the XY plane. The instantaneous target coordinates are

$$\begin{aligned} x_m &= x_0 + V_x t = x_0 + v_x u \\ y_m &= y_0 + V_y t = y_0 + v_y u \end{aligned} \tag{3}$$

where (x_0, y_0) is position of the target at the moment when $t = 0$ (corresponding to the aperture center), $(v_x, v_y) = (V_x/V_0, V_y/V_0)$ is the normalized velocity.

The instantaneous range from the radar to the moving target is identified via

$$R_t(u) = \sqrt{(u - x_m)^2 + (Y_0 - y_m)^2 + Z_0^2}. \tag{4}$$

By inserting Equation (3), Equation (4) becomes

$$R_t(u) = \sqrt{(mu - x_s)^2 + (Y_0 - y_s)^2 + Z_0^2} \tag{5}$$

where

$$
\begin{aligned}
m &= \sqrt{(1 - v_x)^2 + v_y^2} \\
x_s &= \frac{x_0(1 - v_x) + (Y_0 - y_0)v_y}{m} \\
y_s &= Y_0 - \frac{-x_0 v_y + (Y_0 - y_0)(1 - v_x)}{m}
\end{aligned}
\tag{6}
$$

From (5), we can see that the moving target with constant velocity has the identical phase history with the particular stationary target located at (x_s, y_s) but with a scaled sensor velocity.

2.2. SAR Image-error-spectrum Model of Moving Target

Assume that the stationary terrain is described by a complex scattering density $f(x, y)$. Radar located at (u, Y_0, Z_0) in the spatial domain illuminates the target area with large bandwidth signal $p(\tau)$. The radar radiation pattern is assumed to be omni-directional. The SAR echo signal can be expressed as

$$s(u, \tau) = \iint f(x, y) p\left(\tau - 2\sqrt{(x - u)^2 + (y - Y_0)^2 + Z_0^2}/c\right) dx dy \tag{7}$$

where $2\sqrt{(x - u)^2 + (y - Y_0)^2 + Z_0^2}/c$ is the round-trip delay from the radar to the target at position (x, y).

SAR image formation can be thought of as a linear transformation T_{IF}, which maps the echoed data into image data, attempting to recover the original terrain scattering amplitude

$$g(x, y) = T_{IF}\{s(u, \tau)\} \approx f(x, y). \tag{8}$$

The 2-D Fourier transform of image $g(x, y)$ is referred to as *image spectrum*

$$G(k_x, k_y) = \iint g(x, y) \exp(jk_x x + jk_y y) dx dy. \tag{9}$$

For a single stationary point scatter with unit amplitude at position (x_0, y_0), complex scatter function is $f(x, y) =$

$\delta\left(x - x_0, y - y_0\right)$. After SAR processing, its image spectrum is expected as

$$G_0\left(k_x, k_y\right) = \begin{cases} \exp\left(jx_0 k_x + jy_0 k_y\right) & \left(k_x, k_y\right) \in \Omega \\ 0 & \left(k_x, k_y\right) \notin \Omega \end{cases} \quad (10)$$

where Ω is the support region of spatial frequency (wavenumber) domain.

For the moving target p_m, we use (10) to define the ideal image spectrum, which implies that the target is perfectly focused and located at (x_0, y_0). However due to its motion, the moving target, after SAR image formation, almost always appears defocused and located at a false location in the image. In the spectrum domain, this fact can be described by a multiplicative error term that interferes with the ideal image spectrum

$$G_m\left(k_x, k_y\right) = G_0\left(k_x, k_y\right) \cdot G_\varepsilon\left(k_x, k_y\right) \quad (11)$$

In (11), the error term $G_\varepsilon\left(k_x, k_y\right)$ is referred to as *image-error-spectrum* of the moving target. It is worthwhile to note that approximation in SAR image formation, for example, the plane wavefront approximation in PFA, will also result in error, which included in $G_\varepsilon\left(k_x, k_y\right)$.

3. IMAGE-ERROR-SPECTRUM OF MOVING TARGET

For the PFA, the classic theory of radar imaging formulates it by indicating an intrinsic, but simple Fourier transform relationship between the complex reflectivity of the illuminated scene and the collected data (after motion compensation to scene center). PFA performs this Fourier transform by interpolation of the nominally polar samples onto a 2-D Cartesian raster followed by a 2-D FFT. In practice, the mostly adopted implementation of 2-D interpolation is the separable 1-D range and azimuth resampling. In this traditional PFA, the wavefront curvature effect is not considered. However, we must point out that relative to the stationary scene, the moving target causes even severer wavefront curvature effect. We will take this effect into account in the following discussion.

The input signal of moving target to PFA processing is expressed as Equation (2). The first step is to perform range resampling on this signal, which results in [14]

$$S_R\left(u, k_y\right) = C \cdot \exp\left\{jk_y \frac{R_\Delta}{\cos\varphi \cos\theta}\right\} \quad (12)$$

where $k_y = \frac{4\pi}{c}(f_c + f_\tau)\cos\varphi_0$ is the cross-track spatial frequency. Note that k_y is offset from zero, and is centered about $k_{yc} = \frac{4\pi}{c}f_c\cos\varphi_0$. In (12), both R_Δ and $\cos\varphi\cos\theta$ are functions of u. To perform the azimuth analysis, it is helpful to expand $\frac{R_\Delta}{\cos\varphi\cos\theta}$ into a series in u/Y_0. By using the Taylor expansion, and meanwhile ignoring the cubic and higher order terms, $\frac{R_\Delta}{\cos\varphi\cos\theta}$ can be expanded as

$$\frac{R_\Delta}{\cos\varphi\cos\theta} \approx y_0 + x_0\frac{u}{Y_0} + c_0 + c_1\frac{u}{Y_0} + c_2\left(\frac{u}{Y_0}\right)^2 \tag{13}$$

where $y_0 + x_0\frac{u}{Y_0}$ are the desired basic imaging terms for focusing the moving target, $c_0 + c_1\frac{u}{Y_0} + c_2\left(\frac{u}{Y_0}\right)^2$ are the undesired terms resulted from the approximation of image formation and the motion of target. The coefficients can be expressed as

$$
\begin{aligned}
c_0 &= \frac{1}{2}\left(-x_0^2 - y_0^2 + y_0^2\cos^2\varphi_0\right)/Y_0 \\
c_1 &= -x_0 v_x - \left(y_0\sin^2\varphi_0 - Y_0\right)v_y + x_0 y_0\cos^2\varphi_0/Y_0 \\
c_2 &= \frac{1}{2}\Big\{-\left(m^2 - 1\right)Y_0 \\
&\quad + \cos^2\varphi_0\left[(x_0 + Y_0 v_y)^2 - y_0^2\cos^2\varphi_0 + 2Y_0 y_0 v_x\right]/Y_0\Big\}
\end{aligned}
\tag{14}
$$

which are derived in Appendix A.

With (13), the range-resampled signal in (12) becomes

$$S_R(u, k_y) = C\cdot\exp\left\{jk_y\left(y_0 + x_0\frac{u}{Y_0} + c_0 + c_1\frac{u}{Y_0} + c_2\left(\frac{u}{Y_0}\right)^2\right)\right\} \tag{15}$$

The azimuth resampling is a range frequency dependent slow time rescaling procedure, which can also be interpreted as a keystone transform [15]. This keystone transform is formulated as

$$S_A(u, k_y) = S_R\left(\frac{k_{yc}}{k_y}u, k_y\right) = S_R\left(\frac{f_c}{f_c + f_\tau}u, k_y\right) \tag{16}$$

which results in the image spectrum

$$
\begin{aligned}
G_m(k_x, k_y) &= S_A(u, k_y) \\
&= C\cdot\exp\left\{j\left(y_0 k_y + x_0\frac{k_c u}{Y_0} + c_0 k_y + c_1\frac{k_c u}{Y_0} + \frac{c_2}{k_y}\left(\frac{k_c u}{Y_0}\right)^2\right)\right\} \\
&= C\cdot\exp\left\{j\left(y_0 k_y + x_0 k_x + c_0 k_y + c_1 k_x + \frac{c_2}{k_y}(k_x)^2\right)\right\} \tag{17}
\end{aligned}
$$

where $k_x = \frac{k_c u}{Y_0}$ is the along-track spatial frequency. Unlike the cross-track spatial frequency, the along-track spatial frequency in (17) has an unbiased support region, i.e., its center $k_{xc} = 0$, because the variable u is centered at zero. Meanwhile all the targets posses the same support region which is bounded with $|k_x| \leq \pi/\rho_a$, where ρ_a is the along-track spatial resolution.

Using (10), (11) and (17), we obtain the image-error-spectrum

$$G_\varepsilon(k_x, k_y) = C \cdot \exp\left[j\left(c_0 k_y + c_1 k_x + \frac{c_2}{k_y}k_x^2 \right) \right]. \qquad (18)$$

When ignoring the high order terms, the Taylor series expansion of (18) about in the vicinity of $(k_x, k_y) = (k_{xc}, k_{yc})$ is

$$\begin{aligned}
G_\varepsilon(k_x, k_y) = {}& C' \cdot \exp\Big\{ -j\Big[a_{10}(k_x - k_{xc}) + a_{01}(k_y - k_{yc}) \\
& + a_{20}(k_x - k_{xc})^2 + a_{11}(k_x - k_{xc})(k_y - k_{yc}) \\
& + a_{02}(k_y - k_{yc})^2 \Big] \Big\}
\end{aligned} \qquad (19)$$

where

$$a_{10} = c_1 = -x_0 v_x - \left(y_0 \sin^2 \varphi_0 - Y_0\right) v_y + \frac{x_0 y_0 \cos^2 \varphi_0}{Y_0} \qquad (20\text{a})$$

$$a_{01} = c_0 = \frac{-\left(x_0^2 + y_0^2\right) + y_0^2 \cos^2 \varphi_0}{2Y_0} \qquad (20\text{b})$$

$$\begin{aligned}
a_{20} = \frac{c_2}{k_{yc}} = {}& \frac{1}{2k_{yc}}\Big\{ -\left(m^2 - 1\right) Y_0 \\
& + \frac{\cos^2 \varphi_0}{Y_0}\left[(x_0 + Y_0 v_y)^2 - y_0^2 \cos^2 \varphi_0 + 2Y_0 y_0 v_x \right] \Big\}
\end{aligned} \qquad (20\text{c})$$

$$a_{11} = 0 \qquad (20\text{d})$$

$$a_{02} = 0 \qquad (20\text{e})$$

In (20), the coefficients of linear phase terms determine target positioning error in the image, where a_{10} is related to azimuth positioning error and a_{01} to range positioning error; the quadratic coefficients determine the defocusing effect, where a_{20} is related to azimuth defocus, a_{02} to range defocus, and a_{11} to 2-D defocusing (also known as residual linear range walk).

4. SAR SIGNATURES OF MOVING TARGET

The SAR signatures of moving target can be derived from the target image-error-spectrum. Equation (19) represents the image-error-

spectrum of moving target after PFA processing. As is stated in the previous section, the linear phase terms in the image-error-spectrum carry the phase information related to the displacement of moving target from the expected position; the quadratic terms in k_x and k_y cause defocus in azimuth and range, respectively; and the coupling terms of k_x and k_y, corresponds to the residual linear range migration.

4.1. Geometric Displacement of Moving Target

Moving target has no fixed position. However, after SAR processing, we hope that it locates at a specific position, which is referred to nominal position in this paper, for example, the instantaneous position of target when at aperture center. Thus, after SAR processing, the difference between the actual geometrical center position of moving target and this nominal position is referred to as the *geometric displacement*. The coefficients of linear terms in error spectrum indicate these displacements.

For PFA, the geometric displacements result from not only the target's motion, but also the plane wavefront approximation. The azimuth displacement is decided by a_{10} in Equation (20a), in which the term $x_0 y_0 \cos^2 \varphi_0 / Y_0$ is due to the wavefront curvature, and the term $-x_0 v_x - \left(y_0 \sin^2 \varphi_0 - Y_0 \right) v_y$ is induced by the motion of target. It is clear that, besides the well-known Doppler shift effect $Y_0 v_y$ resulted from radial motion, along-track motion also causes azimuth displacement, although it is usually far less than $Y_0 v_y$. Displacement in range is decided by a_{01}. One surprising result found in Equation (20b) is that, the range displacement, which is independent of the target's motion, has the same size with one of the stationary target located at nominal position (x_0, y_0). From [11], we know that any target moving at a constant velocity has a similar phase history with a stationary target located at a specific position, which rotated an angle about the sensor while keeping constant radial range. In PFA image, on the other hand, due to wavefront curvature, two targets with the same radial range from sensor have the same range position. Thus, these two effects tend to cancel each other.

4.2. Residual Range Migration of Moving Target

For SAR image formation algorithms, the correction of range cell migration (RCM) is a key issue to be considered. One shortcoming of the conventional SAR approach, lies in its image processing that, by design, focuses on a stationary target scene, while a moving target introduces additional range migration which the SAR image formation algorithms don't take into account. However, we will see

from the following analysis that part of this additional migration can be naturally corrected during the SAR focusing process, although different image formation algorithms might have different capability for range migration correction. Consequently, the well-known limitation that the RCM of moving target during the coherent processing interval is expected not to exceed a fraction of a range resolution cell [8] can be alleviated, and only the residual range migration, which is much less than the original one, is limited not to exceed a fraction of a range resolution cell.

In the image-error-spectrum, the coupling terms of k_x and k_y are related to the residual range migration. When the relative bandwidth of transmitted signal is sufficiently small, the high order phase terms in the image-error-spectrum can be neglected. Therefore, the only residual range migration that we are concerned is the residual linear range walk.

We can see from (20d) that, the coefficient of the coupling term a_{11} is zero. It means that all the linear range walk of moving target is corrected, although no specific additional processing is employed. This phenomenon of linear range walk elimination can be also explained by considering the azimuth interpolation process of the PFA as the well-known keystone transform [15], which is originally used to correct unknown linear range walk of the moving target.

4.3. Focus Property of Moving Target

Apart from the residual range migration, the quadratic phase terms are the main causes related to the defocusing effect. In the image-error-spectrums presented in (19), the quadratic terms are only related to k_x, which suggests that the defocusing effect occurs only in the along-track direction.

After PFA processing, the residual quadratic phase error is $a_{20}k_x^2$. The maximum phase error, which can be evaluated at the edges of the azimuth spatial frequency, can be expressed as

$$
\begin{aligned}
\Phi_{QPE} &= \frac{1}{2k_{yc}} \left\{ -\left(m^2 - 1\right) Y_0 \right. \\
&\quad \left. + \frac{\cos^2 \varphi_0}{Y_0} \left[(x_0 + Y_0 v_y)^2 - y_0^2 \cos^2 \varphi_0 + 2Y_0 y_0 v_x \right] \right\} \left(\frac{\pi}{\rho_a} \right)^2 \\
&= \frac{1}{2k_{yc}} \left\{ \left(2v_x - v_x^2 - v_y^2 \sin^2 \varphi_0 \right) Y_0 \right. \\
&\quad \left. + \frac{\cos^2 \varphi_0}{Y_0} \left[x_0^2 - y_0^2 \cos^2 \varphi_0 + 2Y_0 \left(y_0 v_x + x_0 v_y \right) \right] \right\} \left(\frac{\pi}{\rho_a} \right)^2 . \quad (21)
\end{aligned}
$$

Assuming that scene radius is r_0, we can further infer that the right-hand side of Equation (21) has an upper bound

$$
\Phi_{QPE}^{\max} = \frac{\pi^2}{2\rho_a^2 k_{yc}} \Bigg\{ \left(2|v_x| + v_x^2 + v_y^2 \sin^2 \varphi_0\right) Y_0 \\
+ \frac{\cos^2 \varphi_0}{Y_0} \left[r_0^2 + 2Y_0 r_0 \left(|v_x| + |v_y|\right)\right] \Bigg\}. \tag{22}
$$

If the QPE allowance is set to be $\pi/2$, i.e., $\Phi_{QPE}^{\max} \leq \pi/2$, we have

$$
\frac{\pi^2}{2\rho_a^2 k_{yc}} \Bigg\{ \left(2\,|v_x| + v_x^2 + v_y^2 \sin^2 \varphi_0\right) Y_0 + \frac{\cos^2 \varphi_0}{Y_0} \left[r_0^2 + 2Y_0 r_0 \left(|v_x| + |v_y|\right)\right] \Bigg\} \\
\leq \pi/2. \tag{23}
$$

Solving Equation (23), we obtain an estimate for allowable scene radius r_0 of

$$
r_0 \leq - \left(|v_x| + |v_y|\right) Y_0 + \frac{Y_0}{\cos \varphi_0} \\
\sqrt{\frac{\rho_a^2 k_{yc}}{\pi Y_0} + \left(|v_x| + |v_y|\right)^2 \cos^2 \varphi_0 - \left(2\,|v_x| + v_x^2 + v_y^2 \sin^2 \varphi_0\right)}. \tag{24}
$$

for the moving target with normalized velocity v_x and v_y.

Figure 2 illustrates this relationship between the allowable scene size (ASS) and the normalized velocity of moving target for simulation parameter listed in Table 1. For target with azimuth motion ($v_x \neq 0$, $v_y = 0$), ASS decreases rapidly, as illustrated in Fig. 2(a). For example, when azimuth normalized velocity v_x goes beyond 0.0026, the ASS becomes zero. Therefore, no targets with velocity beyond this one in the scene can be focused. On the other hand, for target with range motion ($v_x = 0$, $v_y \neq 0$), as illustrated in Fig. 2(b), there is still a large focus region available. For instance, even when range normalized velocity v_y reaches 0.1, the allowable focused scene radius still has size of about $700\,\mathrm{m}$.

5. SIMULATIONS

In this section, point target simulation is employed to validate the presented analysis. Parameters outlining the simulation are listed in Table 1. There are four point targets moving with constant velocity in the ground plane, whose motion parameters are illustrated in Fig. 3. The target's instantaneous position at aperture center is referred
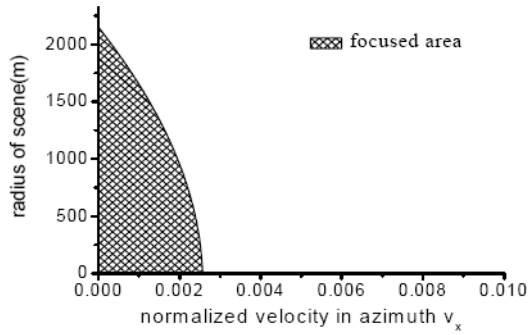
(a)
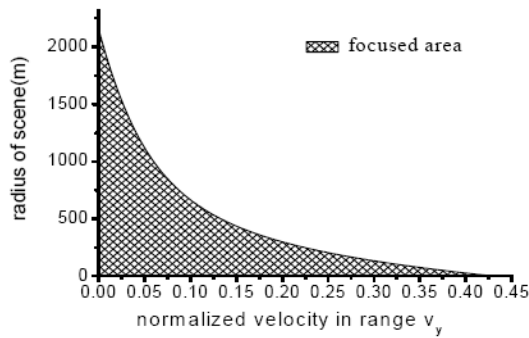
(b)

Figure 2. Focused scene radius versus (a) normalized azimuth velocity and (b) normalized range velocity for moving target in PFA.

Table 1. Simulation parameters.

Parameter description	Value
Carrier frequency	10 GHz
Resolution (range×azimuth)	1 m × 1 m
Synthetic aperture time	4.5 s
Squint angle	0° (broadside)
Scene center range at aperture center	30000 m
Altitude	3000 m
Forward velocity of aircraft	100 m/s

to as the nominal position, which is the reference when we discuss the geometric displacement. All the targets have different motion parameters, among which, target A, B, and D all traverse far more than one range resolution cell during the aperture time due to the radial motion.
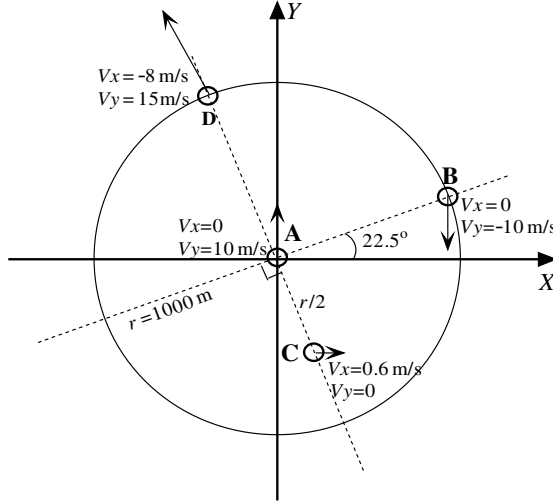

Figure 3. Arrangement of the simulated point targets.

Table 2. Geometric displacement of moving target.

	A	B	C
Theoretical	(2985.0, 0.0)	(−2972.9, −14.3)	(−4.1, −0.7)
Measurement	(2984.4, 0.0)	(−2972.3, −14.6)	(−4.6, −0.6)

For each target, the 2-D impulse response function (IRF) after PFA processing are presented in Fig. 4. In the following, we will give a detailed analysis on their signatures, where target A, B, and C are selected to validate the geometric displacement and focus property, target D is used to show the difference in linear range walk correction between PFA and other image formation algorithms.

Table 2 gives the geometric displacement of moving target after PFA processing. In the table, the theoretical value is derived from the linear phase term coefficients in the image-error-spectrum, while the measured value is from the SAR image. The experimental results show
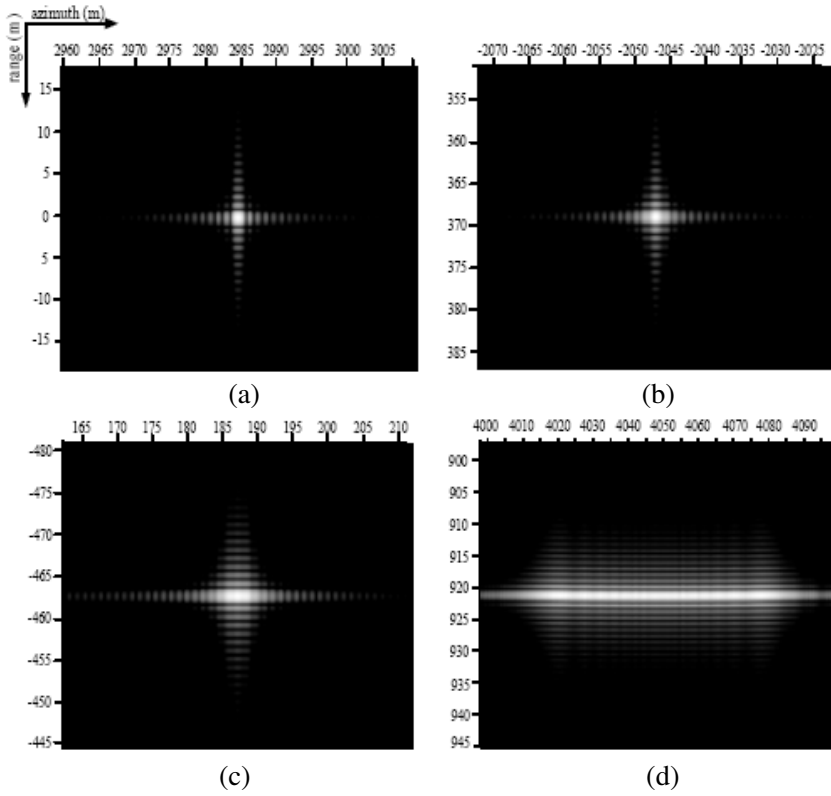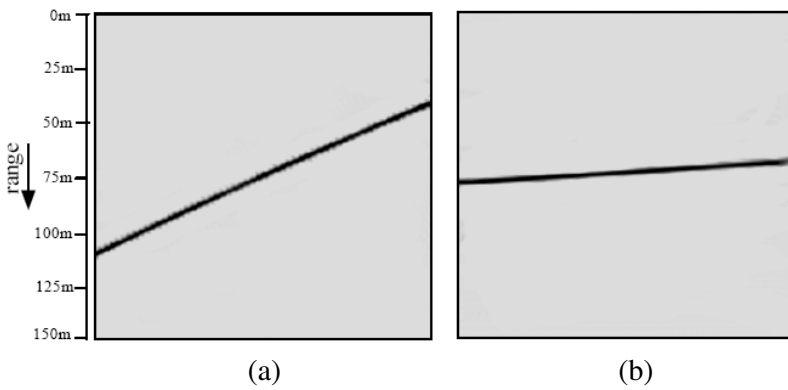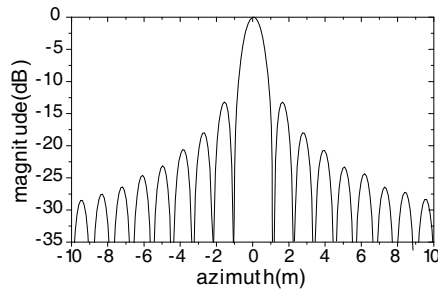
Figure 4. The 2-D IRF of moving target obtained after PFA processing. (a) target A; (b) target B; (c) target C; (d) target D.
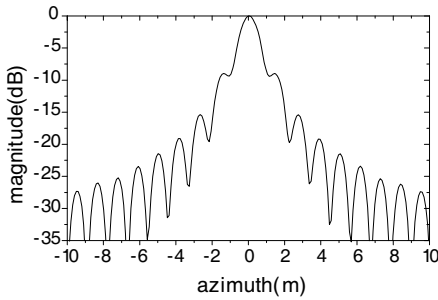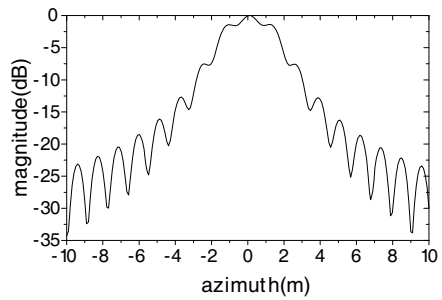
(c)

Figure 5. Range compressed image of target D after (a) linear RD; (b) RMA; (c) PFA.

(a)

(b)

(c)

Figure 6. Azimuth profile of point target response. (a) target A; (b) target B; (c) target C.

that data determined by experiments are in good agreement with the theoretical calculated results.

Due to the keystone transform embedded in azimuth interpolation, PFA can correct the linear range walk for moving targets with different

motion parameters. This property can be clearly seen from Fig. 4. Furthermore, to show the difference in linear range walk correction for different image formation algorithms, Fig. 5 gives the range compressed images of target D after three different image formation algorithms, i.e., linear RD, RMA, and PFA. The moving target's range walk is not treated at all in Fig. 5(a), since Linear RD is a 2-D separable algorithm. However, after RMA processing, part of linear range walk is corrected. Especially, after PFA processing, the linear range walk is corrected completely.

From our analysis, we know that the motion of target only introduce azimuth defocus when the residual range migration can be neglected. Thus, in Fig. 6, we give the azimuth profile of the 2-D IRF of target A, B and C, which corresponding literally to the theoretical QPE (according to Equation (21), their QPE are 0.04 rad, 1.92 rad, and 4.09 rad, respectively).

6. CONCLUSION

In this work, the image-error-spectrum of moving target after PFA processing is derived. Based on this error spectrum, the SAR signatures of moving target, such as geometric displacement, residual range migration and defocus, are presented.

In 2-D separable SAR processing, the additional range migration and phase error caused by target's motion are not treated at all. However, after high resolution SAR processing, the additional range migration and phase error can be partly corrected. Especially, after PFA processing, the linear range walk can be eliminated totally. Therefore, the well-known limitation on range migration for moving target [8] can be alleviated when PFA is employed as the SAR image formation algorithm in SAR/GMTI system.

APPENDIX A.

In this appendix, we derive the Taylor series expansion of $\frac{R_\Delta}{\cos\varphi\cos\theta}$ in Equation (13).

For a target located at (x_m, y_m) on the XY plane in Fig. 1, the differential range is

$$R_\Delta \doteq \frac{\vec{R}_a \cdot \vec{r}_t}{R_a} - \frac{r_t^2}{2R_a} + \frac{\left(\vec{R}_a \cdot \vec{r}_t\right)^2}{2R_a^3} \qquad (A1)$$

where

$$R_{basic} = \frac{\vec{R}_a \cdot \vec{r}_t}{R_a} = x_m \cos\varphi \sin\theta + y_m \cos\varphi \cos\theta \qquad (A2)$$

is the basic imaging terms,

$$
\begin{aligned}
R_{curve} &= -\frac{r_t^2}{2R_a} + \frac{(\vec{R}_a \cdot \vec{r}_t)^2}{2R_a^3} \\
&= \frac{-(x_m^2 + y_m^2) + (x_m \cos\varphi \sin\theta + y_m \cos\varphi \cos\theta)^2}{2R_a} \qquad (A3)
\end{aligned}
$$

is the wavefront curvature terms.

For moving target, inserting the time-variant coordinates in Equation (3), we can get

$$\frac{R_{basic}}{\cos\varphi \cos\theta} = x_m \tan\theta + y_m = y_0 + (x_0 + Y_0 v_y)\left(\frac{u}{Y_0}\right) + Y_0 v_x \left(\frac{u}{Y_0}\right)^2 \qquad (A4)$$

$$\frac{R_{curve}}{\cos\varphi \cos\theta} = \frac{-\left((x_0 + v_x u)^2 + (y_0 + v_y u)^2\right) + \cos^2\varphi \cos^2\theta \left((x_0 + v_x u)\frac{u}{Y_0} + (y_0 + v_y u)\right)^2}{2Y_0}. \qquad (A5)$$

In Equation (A5), the variable φ and θ are still function of u. To facilitate the Taylor series expansion, it is necessary to have expression $\cos^2\varphi \cos^2\theta$ in terms of u. Accounting the imaging geometry, the following relationship existed

$$\cos^2\varphi \cos^2\theta = \frac{1}{1 + \tan^2\varphi_0 + \tan^2\theta} = \frac{1}{1 + \tan^2\varphi_0 + u^2/Y_0^2}. \qquad (A6)$$

Inserting Equation (A6) into Equation (A5), then perform the Taylor series expansion, we can get

$$
\begin{aligned}
\frac{R_{curve}}{\cos\varphi \cos\theta} &= \frac{-\left(x_0^2 + y_0^2\right) + y_0^2 \cos^2\varphi_0}{2Y_0} \\
&\quad + \left[-x_0 v_x - y_0 v_y + (x_0 + Y_0 v_y) y_0 \cos^2\varphi_0/Y_0\right] \frac{u}{Y_0} \\
&\quad + \frac{1}{2} \left\{ -\left(v_x^2 + v_y^2\right) Y_0 + \cos^2\varphi_0 \left[(x_0 + Y_0 v_y)^2 \right. \right. \\
&\quad \left. \left. - y_0^2 \cos^2\varphi_0 + 2Y_0 y_0 v_x\right]/Y_0 \right\} \left(\frac{u}{Y_0}\right)^2 \qquad (A7)
\end{aligned}
$$

where cubic and higher order terms are ignored.

Combined Equations (A4) and (A7), the Taylor series expansion of $\frac{R_\Delta}{\cos\varphi\cos\theta}$ can be expressed as

$$\frac{R_\Delta}{\cos\varphi\cos\theta} = y_0 + x_0\frac{u}{Y_0} + c_0 + c_1\frac{u}{Y_0} + c_2\left(\frac{u}{Y_0}\right)^2 \tag{A8}$$

where

$$\begin{aligned}
c_0 &= \frac{1}{2}\left(-x_0^2 - y_0^2 + y_0^2\cos^2\varphi_0\right)/Y_0 \\
c_1 &= -x_0 v_x - \left(y_0\sin^2\varphi_0 - Y_0\right)v_y + x_0 y_0\cos^2\varphi_0/Y_0 \\
c_2 &= \frac{1}{2}\Big\{-\left(m^2 - 1\right)Y_0 + \cos^2\varphi_0\Big[(x_0 + Y_0 v_y)^2 \\
&\quad - y_0^2\cos^2\varphi_0 + 2Y_0 y_0 v_x\Big]/Y_0\Big\}
\end{aligned} \tag{A9}$$

REFERENCES

1. Storvold, R., E. Malnes, and Y. Larsen, "SAR remote sensing of snow parameters in Norwegian areas-current status and future perspective," *Journal of Electromagnetic Waves and Applications*, Vol. 20, No. 13, 1751–1759, 2006.
2. Chan, Y. K. and S. Y. Lim, "An introduction to Synthetic Aperture Radar (SAR)," *Progress In Electromagnetics Research B*, Vol. 2, 27–60, 2008.
3. Storvold, R., E. Malnes, Y. Larsen, K. A. Hogda, and S. E. Hamran, "SAR remote sensing of snow parameters in norwegian areas-current status and future perspective," *Journal of Electromagnetic Waves and Applications*, Vol. 20, No. 13, 1751–1759, 2006.
4. Nie, X., D. Y. Zhu, and Z. D. Zhu, "Application of synthetic bandwidth approach in SAR polar format algorithm using the deramp technique," *Progress In Electromagetics Research*, PIER 80, 447–460, 2008.
5. Wu, B.-I., M. Yeuing, and Y. Hara, "Insar heigh inversion by using 3-D phase projection with multiple baselines," *Progress In Electromagnetics Reseach*, PIER 91, 173–193, 2009
6. Lim, T. S., C.-S. Lim, and V. C. Koo, "Autofocus algorithm performance evaluations using an integrated SAR product simulator and processor," *Progress In Electromagnetics Reseach B*, Vol. 3, 315–329, 2008.
7. Ebrahimi-Ganjeh, M. A. and A. R. Attari, "Study of water bolus effect on SAR penetration depth and effective field size for local

hyperthermia," *Progress In Electromagnetics Reseach B*, Vol. 4, 273–283, 2008.

8. Raney, R. K., "Synthetic aperture radar imaging radar and moving targets," *IEEE Transactions on Aerospace and Electronic Systems*, Vol. 7, No. 3, 499–505, 1971.

9. Freeman, A. and A. Currie, "Synthetic aperture radar (SAR) images of moving targets," *GEC Journal of Research*, Vol. 5, No. 2, 106–115, 1987.

10. Chen, V. C., R. Lipps, and M. Bottoms, "Advanced synthetic aperture radar imaging and feature analysis," *Proc. of IEEE International Radar Conference*, 22–29, 2003.

11. Minardi, M. J. and E. G. Zelnio, "Comparison of SAR based GMTI and standard GMTI in a dense target environment," *Proc. of SPIE*, 2006.

12. Jao, J. K., "Thoery of synthetic aperture radar imaging of a moving target," *IEEE Transactions on Geoscience and Remote Sensing*, Vol. 39, No. 9, 1984–1992, 2001.

13. Yegulalp, A. F., "Analysis of SAR image formation s for stationary and moving targets," MIT Technical Report, 2002.

14. Doerry, A. W., "SAR processing with stepped chirps and phased array antennas," Sandia Report, 2006.

15. Perry, R. P., R. C. Dipietro, and R. L. Fante, "SAR imaging of moving targets," *IEEE Transactions on Aerospace and Electronic Systems*, Vol. 35, No. 1, 188–200, 1999.